Karlsruhe Institute of Technology

Investigation of the long term stability of the EDELWEISS muon veto system

(Untersuchung der Langzeitstabilität des EDELWEISS Myon-Veto-Systems)

Bachelorarbeit
von

Chenran Xu

am Institut für Experimentelle Kernphysik

Reviewer: Prof. Dr. Guido Drexlin
Second Reviewer: Dr. Klaus Eitel

Bearbeitungszeit: 01.04.2017 – 30.11.2017

Erklärung zur Selbstständigkeit

Ich versichere, dass ich diese Arbeit selbstständig verfasst habe und keine anderen als die angegebenen Quellen und Hilfsmittel benutzt habe, die wörtlich oder inhaltlich übernommenen Stellen als solche kenntlich gemacht und die Satzung des KIT zur Sicherung guter wissenschaftlicher Praxis in der gültigen Fassung vom 17.05.2010 beachtet habe.

Karlsruhe, den 30.11.2017, _____

Chenran Xu

Als Ansichtsexemplar genehmigt von

Karlsruhe, den 30.11.2017, _____

Prof. Dr. Guido Drexlin

Contents

1. Introduction

Astrophysical and cosmological observations over the last decades indicate the existence of some non-baryonic dark matter. By analyzing the anisotropy of cosmic microwave background, the dark matter energy contribution is estimated to be 27% of the universe [Col16]. Yet no knowledge of the particle constituent of the dark matter is obtained.

A generic class of hypothetical particles, the Weakly Interacting Massive Particle (WIMP), is a prominent candidate for the dark matter. WIMPs are often assumed to have a mass of $\mathcal{O}(100\,\text{GeV})$, with an interaction cross section with ordinary matter of the order of the weak interaction scale.

The EDELWEISS experiment aims to search for a direct signal of elastic scattering of WIMPs on germanium nuclei. Due to the expected low rate of WIMP-nucleus scattering, the main challenge of the experiment is to understand and exclude potentially all the background events.

The detectors are surrounded by multiple layers of external shielding, which absorb and reject background radioactivity. Further backgrounds from the radioactivity of the shielding materials can be discriminated by the simultaneous readout of heat and ionization signals. The remaining neutron background causes a nuclear recoil in detectors, which can hardly be distinguished from a WIMP-signal. The neutrons are produced either by (α, n) reaction from natural radioactivity or by cosmic-ray muons and natural radioactivity. To protect the detectors from the cosmic muon background, EDELWEISS is located in the underground laboratory in Modane (Laboratoire Souterrain de Modane, LSM), where the muon flux is reduced to $5\,\mu/\text{m}^2/\text{d}$ [SAA$^+$13]. The remaining muons are tagged by a muon-veto system of 46 plastic scintillator modules.

Since the start of the EDELWEISS experiment, the scintillator modules as well as the electronics have aged significantly. The goal of this work is to estimate the stability of the muon veto system over a period of several years. Four extra scintillator modules installed in 2010 are also equipped with LEDs allowing to monitor the stability of the system with this special light source.

In chapter 2 the case of dark matter with focus on WIMPs is discussed, followed by a brief description of the general setup of the EDELWEISS experiment. In chapter 3 the setup and the working principle of the muon-veto systemis described. First, in chapter 4 the LED events are analysed to estimate the long term stability of these four modules. Second, in chapter 5 the muon events are selected for the analysis of all modules. Additionally, the effective threshold of each module is determined to estimate the change of the detection efficiency of the muon-veto system.

2. Search for WIMPs with the EDELWEISS experiment

Nowadays, the search for dark matter becomes one of the central topics in astroparticle physics. Numerous experiments aim to search for dark matter. In this chapter, observational evidences of dark matter are given, followed by a description of particle candidates of dark matter with the focus on WIMPs. EDELWEISS is one of the experiments to directly search for dark matter. The general setup and working principle is described.

2.1. Evidences of dark matter

In 1933, while studying the velocity dispersion of galaxies inside the Coma galaxy cluster, F.Zwicky inferred the existence of some kind of unseen mass, which he called *dunkle Materie* (dark matter). Since then, his idea was supported by numerous observations on different scales – e.g. Cosmic Microwave Background(CMB, [Col16]), the Bullet Cluster. The Bullet Cluster (1E 0657-56) consists of two clusters, which collided around 100 Myrs ago. Using gravitational lensing and X-Ray analysis, it is found that the two galaxy concentrations have moved ahead of their plasma clouds, which indicates the existence of weak-interacting dark matter [CBG$^+$06]. In the following a more detailed description of the evidence of dark matter in galaxies is given.

Galaxy rotation curve

Taking a simplified model where almost all the galactic mass is inside a radius R, the rotation velocity of an object at large distance from the galactic centre can be approximated:

$$v(r) = \sqrt{\frac{GM}{r}} \tag{2.1}$$

M denotes the galactic mass, and r the distance to the galactic centre with r > R. Therefore, the velocity is expected to behave as $v \approx r^{-1/2}$ at large distances according to Kepler's law. However, observation of flat rotation curves shows discrepancy from the expectation. In 1980, an extensive study of 21 galaxies suggested that most stars in spiral galaxies have roughly the same orbital velocity, which implies the existence of some kind of unseen matter [RTF80]. Fig 2.1 shows an example of the observed rotation curve of one spiral galaxy. The contribution of baryonic matter (disk and gas) to the velocity decreases with distance, whereas the DM-halo one rises. Together they lead to the observed flat curve at large radius.

It should also be mentioned that there are alternative theories to explain the problem of galaxy rotation curves, such as Modified Newtonian Dynamics (MOND, [Mil83]). Although MOND successfully solves the problem in galactic scale, it cannot cope with the observations at larger scales.
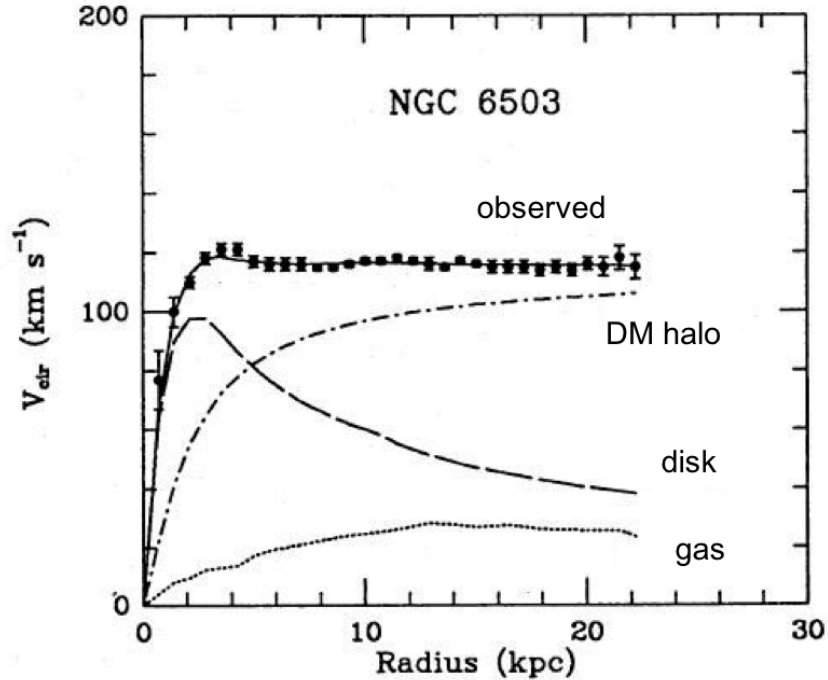
Figure 2.1.: An example of a galaxy rotation curve (NGC 6503). The observed rotation curve is plotted together with the individual components. Extracted from [RTF80].

.

2.2. The WIMP as a dark matter particle candidate

The Λ cold dark matter (ΛCDM) model is a parametrization of the Big Bang model and successfully explains the evolution of the universe. It is therefore often referred to as the standard model of cosmology. As the name suggests, the ΛCDM model contains as most prominent contribution a cosmological constant (denoted with Λ) and cold dark matter, which means that dark matter mostly consist of non-relativistic particles. Also, dark matter is electrically uncharged and mostly collisionless. The DM particles only interact with themselves and other particles through gravitation and weak force. They have to be stable on a cosmological time scale, otherwise they would not exist with such abundance nowadays.

In the Standard Model (SM), no particle satisfies all the properties above. The SM is thus to be extended. There are many hypothetical particles as potential dark matter candidates, e.g. axions, sterile neutrinos, WIMPs. The axion is a hypothetical elementary particle to solve the strong CP problem [PQ77]. Sterile neutrinos are right-handed neutrinos that only interact via gravitation. They would be a candidate of warm dark matter if their mass is in the keV range. The dark matter candidate of interest in this work is called WIMP (weakly interacting massive particle), a generic class of hypothetical particles.

The WIMP is expected to have mass of a few GeV to a few TeV and interact weakly and gravitationally. For sufficiently high temperatures, like in the early universe, the WIMPs are constantly produced and annihilated. As the temperature drops, the WIMPs eventually cease to interact and the particle density remains roughly the same. A promising candidate of WIMPs is the so-called lightest supersymmetric particle (LSP) of the supersymmetric model (SUSY). SUSY is an extension of the standard model where each SM-particle has a SUSY-partner which differs only by a half-integer spin. In many models the LSP turns out to be neutralino, which is the mixture of four SUSY-particles.

Due to the low interaction cross section, WIMPs are extremely hard to detect. They can be detected through different methods. They can be produced by the collision of SM-

particles. WIMPs can also be detected indirectly by measuring the SM-particles produced in self-annihilation of dark matter. Lastly, they can be directly detected by observation of WIMP-nucleus scattering like in the EDELWEISS experiment.

2.3. The EDELWEISS Experiment

The EDELWEISS experiment is dedicated to detect the scattering of WIMPs on ordinary matter at cryogenic temperature. In order to achieve the expected sensitivity down to 10^{-9} pb, the main challenge is to exclude all the backgrounds induced by radioactivity or cosmic rays. The general setup of the experiment and the possible backgrounds are summarized in section 2.3.1. The remaining backgrounds can be discriminated by measurements of two channels of the signal. This working principle of germanium bolometers is briefly described in section 2.3.2. The problematic muon-induced neutrons, which can hardly be distinguished from the WIMP-signal, are described in detail in chapter 3.

2.3.1. Experimental setup and backgrounds of EDELWEISS-III

The EDELWEISS experiment is located in the underground laboratory of Modane (*Laboratoire Souterrain de Modane*, LSM). Under 1780 meters of rock, the cosmic muon flux is reduced by more than a factor 10^6 to a remaining rate of $5\,\mu/\text{m}^2/\text{d}$ [SAA+13]. The remaining throughgoing muons are tagged with an active muon-veto system, which is the outermost layer of the setup (see fig.2.2). A detailed description and working principle are given in chapter 3.
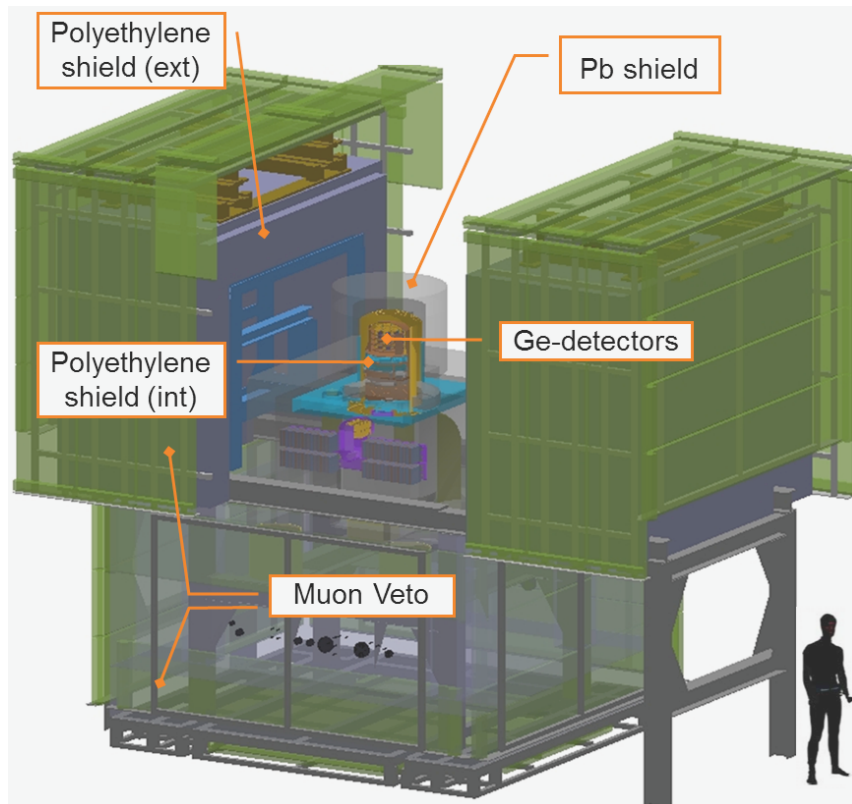
Figure 2.2.: Schematic view of the EDELWEISS experimental setup. In the center are the Ge-bolometers hosted in a cryostat. The cryostat is surrounded by a lead shield, a PE shield and an active muon veto system to minimize the backgrounds. Extracted from [Kéf16].

The next layer is a polyethylene (PE) shield of about 50 cm thickness to attenuate the neutron flux from the radioactivity of rock and experiment materials. The fast neutron flux

with energy above $1\,\mathrm{MeV}$, which produces similar recoils as from WIMPs, is reduced by 5 to 6 orders of magnitude. Next to the PE shield is a lead shield of 20 cm thickness to reduce the ambient γ background. The natural lead contains radioactive isotopes–e.g. ^{210}Pb, ^{238}U and ^{232}Th, which also contribute to the background. To reduce its natural radioactivity, the innermost $2\,\mathrm{cm}$ of the shield is made of Roman lead discovered in a sunken ship. The ^{210}Pb has a half-life of $T_{1/2} = 22\,\mathrm{years}$, so that its abundance is decreased by two orders of magnitude [SAA$^+$13]. Another source of external background is the ^{222}Rn gas in the air which is a decay product of ^{238}U.

The upper part with the cryostat is installed in a clean room with renewing air to minimize the radon level. The space between the lead shield and the cryostat is flushed with filtered air. The upper part of the shieldings are mounted on rails and can be opened in halves to access the cryostat and electronics. Additional layers of PE and lead shields are installed inside the cryostat to reduce the background induced by electronics and cables.

The cryostat is a ^{3}He/^{4}He dilution refrigerator made of low-radioactivity materials. The detectors are enclosed in five thermal screens and the temperature decreases from room temperature over $100\,\mathrm{K}$, $40\,\mathrm{K}$, $4\,\mathrm{K}$, $1\,\mathrm{k}$ to $10\,\mathrm{mK}$. In standard operations, the temperature of the detectors is tuned to $T = (18.000 \pm 0.002)\,\mathrm{mK}$. More detail of the setup can be found in [A$^+$17].

2.3.2. Working principle of Ge Bolometer

The bolometers used in the EDELWEISS experiment are made of high-purity monocrystalline germanium. They are equipped with aluminium ring electrodes and glued with 2 Neutron Transmutation Doped (NTD) sensors.

The thermalized phonon signals are measured via the change of resistance of the NTD Ge sensors. The small temperature rise resulted by an energy deposit E_{rec} is

$$\Delta T = \frac{E_{\mathrm{rec}}}{C(T)} \tag{2.2}$$

by which $C(T)$ is the total heat capacity of the germanium crystal and two NTD sensors. The temperature dependency of the resistance is given by

$$R(T) = R_0 exp\sqrt{\frac{T_0}{T}} \tag{2.3}$$

with characteristic constants $R_0 = \mathcal{O}(0.1\,\Omega)$ and $T_0 = \mathcal{O}(1\,\mathrm{K})$. At the operating temperature of $18\,\mathrm{mK}$, the resistance becomes a few MΩ. The NTD sensors are biased with a square modulated current and the resistance change is obtained by change of the voltage.

For each event, the ionization energy E_{ion} is simultaneously measured. Electron-hole pairs are produced in the germanium crystal for an energy deposit above $2.96\,\mathrm{eV}$. The produced charge carriers are drifted to the biased electrodes and collected.

The discrimination between electron recoils and nuclear recoils is based on the ionization yield Q, defined as the fraction of ionization energy and recoil energy:

$$Q = \frac{E_{\mathrm{ion}}}{E_{\mathrm{rec}}} \tag{2.4}$$

Since the WIMPs and neutrons scatter off nuclei, the required energy to produce a pair of charge carriers is higher than the one of electron recoils. Most energy deposited by nuclear recoils is directly transmitted to phonons, which leads to a generally smaller ionization yield than electron recoils.

The heat and ionization channels are calibrated with the $356\,\mathrm{keV}$ line of $^{133}\mathrm{Ba}$, which induces electron recoils. With the ionization yield of electron recoils set to 1, the neutron ionization yield is determined with a neutron calibration [DBC$^+$01]:

$$Q_\mathrm{n} = 0.16 \cdot (E_\mathrm{rec}[\mathrm{keV}])^{0.18} \tag{2.5}$$

With combination of the heat and ionization measurements, the electron recoils can be distinguished from the neutron recoils. Therefore, the remaining problematic background is neutrons, mostly produced in muon-induced showers or muon-nuclear interactions.

3. Muon detection in EDELWEISS experiment

Despite the rock overburden of LSM which reduces the cosmic muon flux by 6 orders of magnitude, the remaining muons can produce neutrons and mimic WIMP signals. These muons are tagged by an active veto system. The general setup and the working principle of the system is described in this chapter. The description is mainly based on the doctoral thesis of C. Kéfélian [Kéf16].

3.1. Setup of the muon-veto system

The muon-veto system is the outermost layer of shieldings and covers a surface of $100\,\mathrm{m^2}$. As shown in the fig. 3.1, it is made of 46 plastic scintillator modules. The modules are labelled from 1 to 48. Each wall is labelled according to the orientation. The western wall is named "Nemo", which is the name of the neighbour experiment in LSM. The muon-veto is divided in two levels, the upper level made of 30 modules is located in a clean room which hosts the cryostat and the detectors. The lower level has 16 modules. As described in section 2.3.1, the upper level is mounted on rails and can be opened in two parts to grant access to electronics and the cryostat.

To cover the gap resulted from an extension of the cryogenic support line, additional modules M7, M8, M15 and M16 were installed in 2010. The four extra modules are equipped with LEDs to monitor the stability of the system. M7 and M8 have 3 LEDs along their axis, each of M15 and M16 has one LED installed in the middle. M7 and M8 are $2.1\,\mathrm{m}$ long. M15 and M16 are around $1\,\mathrm{m}$ long and cover only partly the opening of the upper part.

All modules have a width of $65\,\mathrm{cm}$ and a thickness of $5\,\mathrm{cm}$. Their lengths vary from $2\,\mathrm{m}$ to $4\,\mathrm{m}$. Due to the opening for electronics and the shorter length of some modules, the overall geometric coverage is 98%. However, a muon going through the gap can partly be detected via the particle showers induced by it or at its exit hitting another module.

A group of four Photomultiplier Tubes (PMT) is installed at each module end. Each PMT group is individually biased with a high voltage (HV). The HV values are typically set around $-1500\,\mathrm{V}$ and only seldom changed over years when an abnormal behaviour was observed in a module. To ensure that the system is fully closed while operating, two lasers measure the position of two halves of the upper part every 15 minutes. One measures the distance from the western wall to M6, the other from the eastern wall to M8. The gap width is calculated by subtracting the two distances.

3.2. Working principle of the muon-veto system

3.2.1. Muon energy deposit in the scintillator modules

The average muon energy at LSM is $< E_\mu >_{\mathrm{LSM}} \approx 260\,\mathrm{GeV}$ [Klu13]. The high energy muons deposit $2\,\mathrm{MeV/cm}$ in the muon-veto modules according to the Bethe formula. Since
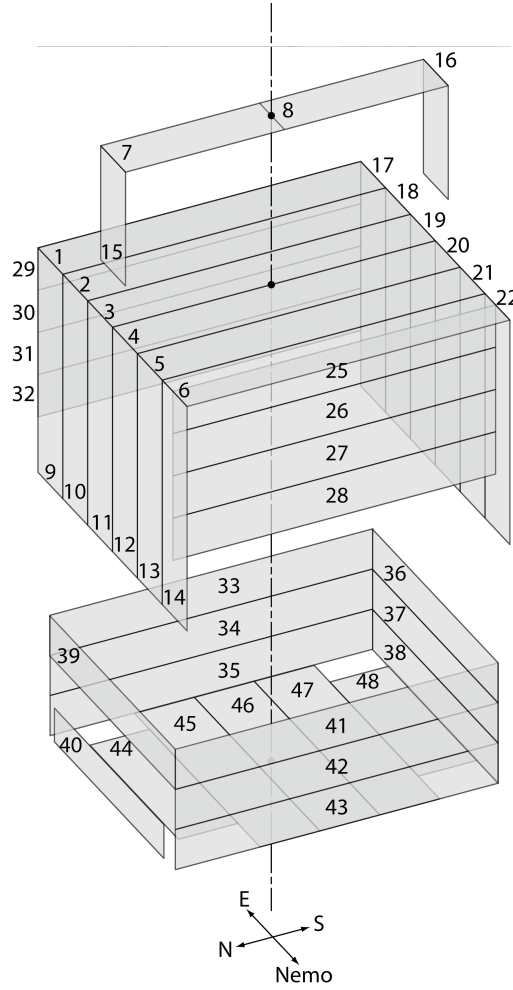
Figure 3.1.: Schematic view of the muon-veto system. Each wall of the system is labelled according to its geometric orientation in the laboratory.

.

the scintillator modules have a thickness of 5cm, the muon energy deposit in a module is typically above 10 MeV. Therefore, the muon events can be separated from the background events with energy deposit normally lower than 4 MeV, which reduces the dead-time of the experiment. The stochastic process of muon energy deposit can be described by a Landau distribution [Lan44]. Such distribution is asymmetric and has a long tail towards the high energy region. To avoid the contribution of large energy deposit from the long tail, the most probable value (MPV) is usually taken to characterize the distribution. The total energy deposit of muon is also dependent on its path length in a module. The spectrum is thus smeared due to the different orientation of modules and the angular distribution of the muon flux. Most muons at LSM have small zenith angle, therefore the muons deposit minimal energy in top and bottom modules and the track length is of the order of the module thickness. It is also possible that a muon goes through the edge of a module, which is called a *grazing muon*. In such case, the muon traverses only partly the module thickness and deposits lower energy.

3.2.2. The electronic readout chain

The data acquisition of the muon-veto system is independent from the bolometer. The muon-veto is only rarely switched off when operation in the clean room is taking place. When a muon goes through the scintillator modules, it deposits energy via different processes and produces scintillation light. The photons reflect in the module and are guided to the

PMT groups. In a PMT group, the photons are then converted to electrons and amplified to a measurable electric signal. Once the signal amplitude is over the trigger threshold, the signal is integrated in the Analog-to-Digital-Converter (ADC) card to obtain the total energy deposit of a muon in a module. At the mean time, the Time-to-Digital-Converter (TDC) card stores the time of the signal. If there is a coincidence of both PMT groups in a module within a 100 ns time window, all non-zero signals of the muon-veto system are stored as one event. After the triggering, there is a dead-time of $\tau = 0.16$ ms when no events can be detected [Sch13]. The trigger threshold is set to 150 mV to ensure the detection efficiency of low energy events without introducing too much dead-time.

3.2.3. Position-dependent light output

In addition to the fluctuation of the muon energy deposit, the light output is also dependent on the position of the interaction in the scintillator modules. Since the light is guided up to 4 m to the PMT group, which is much larger than the attenuation length, the light measured by PMT decreases exponentially with the path length d. The relation can be approximately determined by the Beer-Lambert law:

$$I(d) = I_0 \cdot e^{-\frac{d}{\Lambda_{\text{eff}}}} \tag{3.1}$$

The Λ_{eff} denotes the effective attenuation length and is a detector specific constant. The scintillator modules in EDELWEISS were previously used in the KARMEN experiment. The effective attenuation length was measured to be $\Lambda \approx 600$ cm in 1997/1998 [Rei98]. However, the modules have aged since then. Some of the effects are radiation damages and decrease of the transparency.
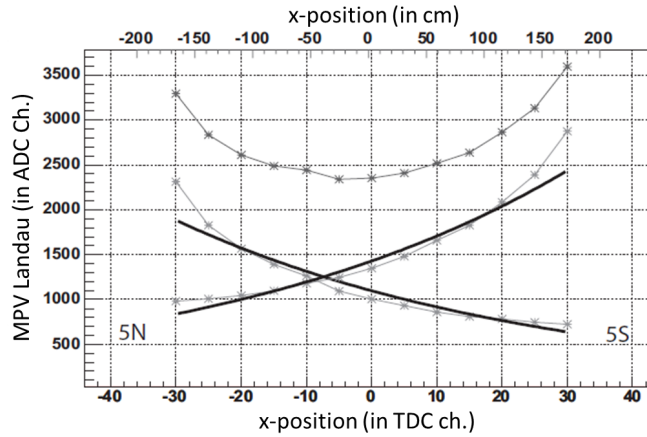
Figure 3.2.: Light measured in the north and south PMT groups of Module 5 and the sum of them. The data are fitted with exponential curves. Extracted from [Hab04].

In 2003/2004, the attenuation lengths of two 4 m modules were measured. Fig. 3.2 shows the measured signal in M5 for two individual PMT groups and the sum of them. As shown in the figure, the light yield varies by a factor of 2 from the near end to the far end. For M5 Λ_{eff} was around 340 cm and for M1 around 200 cm [Hab04]. The measurement shows that the effective attenuation length of scintillator modules has decreased significantly since production, which leads to a decrease of discrimination efficiency for low energy events. This also motivates the importance to analyze the long term stability of the muon-veto system.

3.2.4. Available information of the muon-veto events

The measured events are stored in data files and combined to so-called Runs. Each Run contains up to 99 files, where each file stores 8 hours measurement. This means, one Run usually contains data of one month measurement time. The data in each Run file are converted to a *KData* file. *KData* is a ROOT-based [BR97] data structure and analysis toolkit developed at KIT. It combines the muon-veto data and the bolometer data for coincidence studies [CAA$^+$12]. The data branches relevant in the context of this work and available for the analysis are listed below:

- **ADC:** When triggered, the integrated signal in each PMT group is stored in ADC units. The HVs of each PMT group are calibrated before the experiment to ensure a uniform gain of each module. Since the modules have aged individually, the correspondence between ADC channels and energy in MeV varies from module to module. There is also a digital conversion threshold. For an event with energy deposit below this value, the ADC is not stored and set to -1. The digital threshold is typically 120 ADC channels.

- **TDC:** The arrival time of a signal in each PMT group is stored. By subtracting the two TDC values in one module, the event position can be reconstructed. In the presented work, the TDC values are only used to probe if a PMT group is triggered.

- **PC Time:** The time of each event is stored in units of seconds. For the muon-veto events to be compared with bolometer events, an additional timestamp in 10 μs precision is saved. However, such precision is of no interest in the analysis of the long term stability. Therefore, the event time in seconds is used in the following analysis.

- **DistanceEst, DistanceNemo:** As described before, the gap size of the upper part of the system is measured every 15 minutes. DistanceEst stores the distance from the western wall to M8 (eastern half of the muon-veto) and DistanceNemo stores the distance from western wall to M6 (western-most module of the upper muon-veto). For each event, the distances obtained from the last laser measurement are stored.

- **IsLEDFired:** The LEDs installed on the extra top modules fire every eight hours to monitor the stability of the system. When the event is caused by LED firing, the boolean value IsLEDFired is set to true, allowing a distinction between LED events and other events.

4. Long term behavior of data acquired with LEDs

As described in Chapter 3, the four extra modules added in 2010 covering the gap of the muon-veto system are equipped with LEDs. M7 and M8 have three LEDs: one at the center and the other two symmetrically at the end. M15 and M16 both have one LED installed at the center. The LEDs send out pulses every eight hours. The LED data are used to perform a stability control of the muon-veto system. They are clearly defined in light emission, position and time comparing to muon induced events, therefore the LED events are a good probe to estimate the long term stability of these four modules.

4.1. Data selection

For the following analyses, data of muon-veto Run70 to Run138 are used to analyze the aging effect of the veto system. This corresponds to a date from 24.08.2010 to 28.03.2017. When converting the raw data to ROOT-format, the events induced by LED firing are flagged. Therefore, they are easily separated from other events. The LEDs fire three times every day. Each LED fires 60 pulses in one minute and they fire one after another, which also allows a separation of signals from different LEDs in M7 and M8.

4.2. Data Analysis

The LEDs are fixed on the modules, so the energy spectrum is not smeared by the position dependent light readout. Also, the LEDs are supposed to have constant light output over a short time. Thus the obtained ADC spectrum can be fitted with a gaussian function to get the average ADC values of several series. To increase the statistical power of a single point, events of nine shot series (three days) are combined to perform a gaussian fit. An example of such fit is illustrated in fig.4.1.

The mean ADC values obtained from each gaussian fit are plotted over time. A change of these values over time could be due to various effects, e.g. a decrease of the LED light output, aging of scintillator modules, problem of the PMTs or readout electronics. To identify the contribution of different factors, the values are plotted separately for two PMT groups and three LEDs (for M7 and M8). Linear regressions are made for each data set, see fig.4.2. The lines with different color represent the data from different LEDs. In the following, the result is described in detail for a sample module M8.

As can be seen in the figure, the mean ADC values of the two off-center LEDs differ about 500 to 1000 channels from the far end to the near end. Since M7 and M8 are only half the length of other top modules, such position dependent effects are expected to be even more remarkable in other modules.

In fig.4.2, the error bar of a single data point is the statistical uncertainty given by the gaussian fit. Since most LED events in one fire series have good gaussian form, the statistical
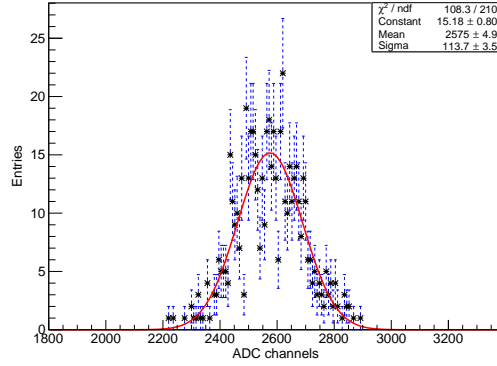
Figure 4.1.: Example of an gaussian fit to nine LED fire series in Module 8, north PMT group. The spectrum is fitted with a log likelihood method in ROOT.

uncertainty is mostly much smaller than the total uncertainty. Several other effects lead to the fluctuation of the ADC value, for example, the switch-on effect of electronics after a long pause. Consequently, the systematic uncertainty can only be approximated. The result of the linear fits are listed in Tab.4.1 with uncertainty. The systematic uncertainty of the slope is estimated by fitting different parts of the time period and taking the difference of the maximum and minimum slopes.

4.2.1. Interpretation of the results

Various effects could lead to the decrease or even increase of the mean ADC value of LED events. First, the transparency of plastic scintillator decreases over time. Assuming that such aging effect is homogeneous in one module, the loss of light output depends on the distance from the event position to the PMT group. This leads to roughly the same decrease for events that have same track length to the PMT group, e.g. LED N to ADC S and LED S to ADC N. Second, the PMTs as well as the junction of scintillator module and PMT group have aged individually, which leads to different variation of ADC values at two ends of a module. Last, the light output of an LED may vary over time and thus leads to the simultaneous change of measured values in two PMT groups.

The slopes of middle LED in two ends of M8 are about the same, implying that the two PMT groups of M8 have aged similarly. Therefore the aging effect of the plastic scintillator can be estimated by subtracting the slope of same LED at the far end from the one at the near end. Furthermore the decrease is noticeably more rapid at earlier stage (about 2010-2011) and becomes flat later. The reason can be that the transparency loss of scintillator is not linear over time. The assumption of linear trend is thus only an approximation. Averaging over time, the decrease due to aging of plastic scintillator is estimated to be ≈ 3 channels/month. During the total period of experiment (about 90 months), the change of ADC values caused by scintillator aging is about 250 channels for M8.

Table 4.1.: Slopes of the linear regressions of 3 LEDs in M8. The first uncertainty is the statistical uncertainty from the linear fit, the second is the estimated systematic uncertainty.

	slope in channels/month		
	LED S	LED M	LED N
ADC N	$-7.26 \pm 0.05 \pm 4.32$	$-1.13 \pm 0.05 \pm 1.06$	$+2.37 \pm 0.07 \pm 3.12$
ADC S	$-3.02 \pm 0.07 \pm 5.50$	$-1.49 \pm 0.06 \pm 2.92$	$+0.59 \pm 0.05 \pm 2.74$
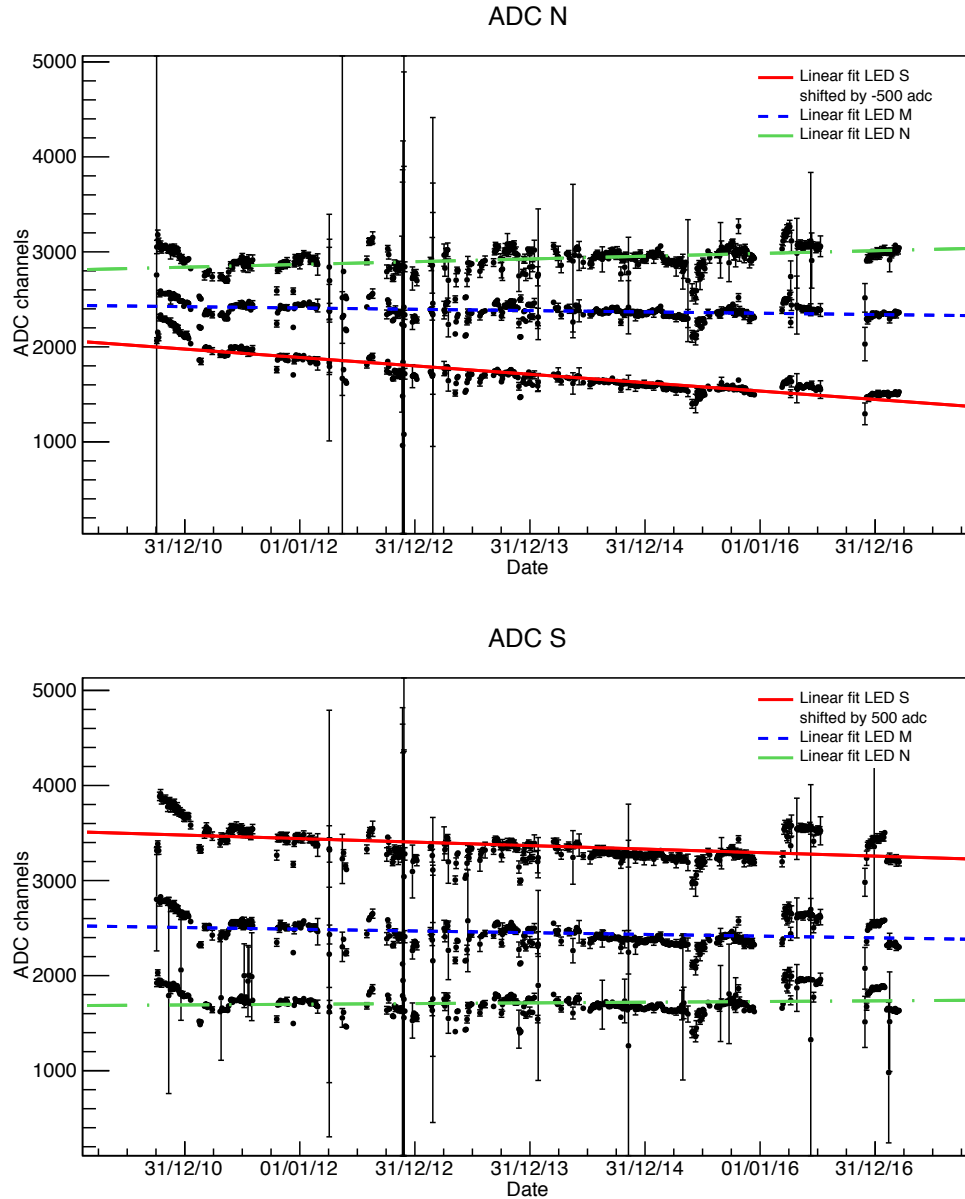
Figure 4.2.: ADC mean values of LED signals over time in Module 8.
The energy deposit of LED signals in ADC channels from Run70 to Run138 are plotted separately for 2 PMT groups (north in upper chart, south in lower chart). The trend of ADC values of different LEDs over time are approximated by linear fits: the green line (LED north), the blue line (LED middle), and the red line (LED south). For clarity reasons, the signals of the south LED are decreased by 500 channels in upper chart and increased by 500 in lower chart.

Same procedure is applied on other three modules M7,M15 and M16 and shows similar results. Since other modules are longer then the four modules, the decrease of ADC values are expected to be more significant. The detection efficiency reduces especially for events to be measured in the far PMT group, as the transportation length of light is longer.

5. Determination of the long term stability using muon events

Analysis of LED events can only be applied on the four extra top modules. To determine the stability of the total muon-veto system, aging of all modules are investigated. In this chapter, the muon-events are selected and analysed. Additionally, the effective threshold of each module is determined using an independent method, which allows to estimate the change of the detection efficiency of the modules.

5.1. Analysis of muon events

5.1.1. Selection of muon-veto data

All the data from Run70 (Aug 2010) to Run138 (Mar 2017) are investigated in the following analysis. Since the goal is to analyse the stability of muon detection in modules, several cuts are applied on the data to ensure a stable condition of the system during the investigated time period and to decrease background events.

First, data taken when the muon-veto system was not fully closed are cut. As described in 3.1, two lasers measure the position of the upper part of the muon-veto every 15 minutes. Time periods when the gap size deviates more than 5 cm from the closed configuration are cut, since the muon-veto system is either fully closed or fully opened. When the system is opened, the detection efficiency of through-going muons decreases and the background rate increases largely, which will lead to a increase of low energy events and .

When the muon-veto system is closed, most muons go through at least 2 modules. Therefore a coincidence in 2 distinct modules is required for selecting muon events. An energy deposit with full information in each module is required–i.e. both TDCs and ADCs have non-zero values. It respectively reduces events caused by secondary particles or natural backgrounds as they mostly deposit less energy than muons. By applying this cut criterium, the event rate in one module is reduced to the order of 10 events/day.

5.1.2. Data analysis

As mentioned in section 3.2, the spectrum of muon energy deposit in modules can be described by a Landau distribution. The ADC values of muon events in a time period are fitted with a Landau distribution and the obtained MPVs in different time periods are used to analyse the long term behaviour of the muon-veto system. The fig. 5.1 shows an example of the Landau fit. Since the muon event rate is low, the obtained ADC values in a two months period are combined to perform each fit.

The MPVs obtained from the Landau fit are plotted over time (see fig. 5.2). Some time periods with too few entries due to the system shutoff are excluded, since no reliable Landau fit can be performed. It is to be noticed that the data points have rather large uncertainty, which is partially due to the smeared spectrum. As explained before, the light output is
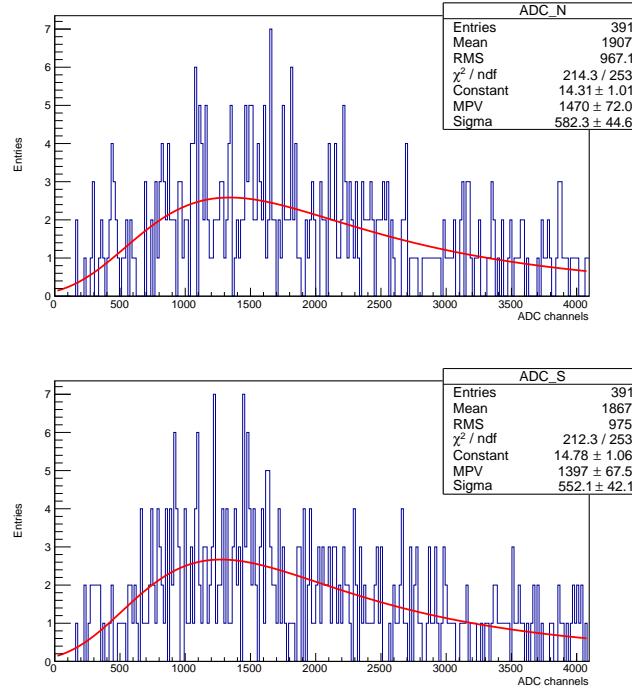
Figure 5.1.: Example of a Landau fit in M6. The fit uses a log likelihood method in ROOT.

strongly position dependent and decreases exponentially with the path length from the interaction point to the PMT group. Furthermore, there are some sudden changes of the MPVs. The reason could be the restart of the muon-veto system after operations.

Table 5.1.: Slopes of the linear regressions of MPVs in example modules M6, M8 and M44. The statistical uncertainty is obtained from the fit program in ROOT.

Module	slope in channels/month	
	ADC N	ADC S
M6	-5.44 ± 1.34	-4.87 ± 1.12
M8	-5.26 ± 0.52	-6.00 ± 0.46
M44	-5.76 ± 3.71	-3.71 ± 1.12

The change of the MPVs are again approximated by a linear regression and the obtained slopes are listed in tab. 5.1. It can be seen that the slopes for two ends in a single module don't vary much from each other, which means that the aging of plastic scintillator is as expected almost symmetric and the electronics of two PMT groups have also aged similarly.

The value obtained in M8 is also listed for comparison with the result from LED data. The decrease of the MPVs is larger than the one of ADC mean values of middle and northern LED events and lies in the uncertainty regions of southern LED events. The abnormal increase of ADC mean values of LED S in M8 (see tab.4.1) is not to be found in the data obtained from muon events. Thus it can be concluded that the problem is merely due to the behaviour of the LED but not the scintillator module.

Despite the various effects that may lead to a sudden change of the ADC value, the MPVs of the Landau spectrum in all 46 modules show a general decrease of several hundred ADC channels since 2010.
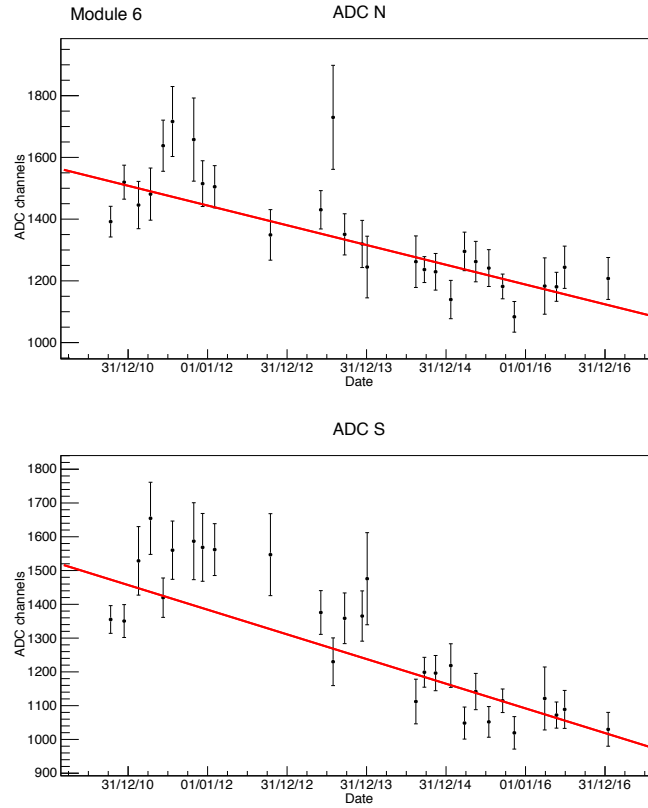
(a)
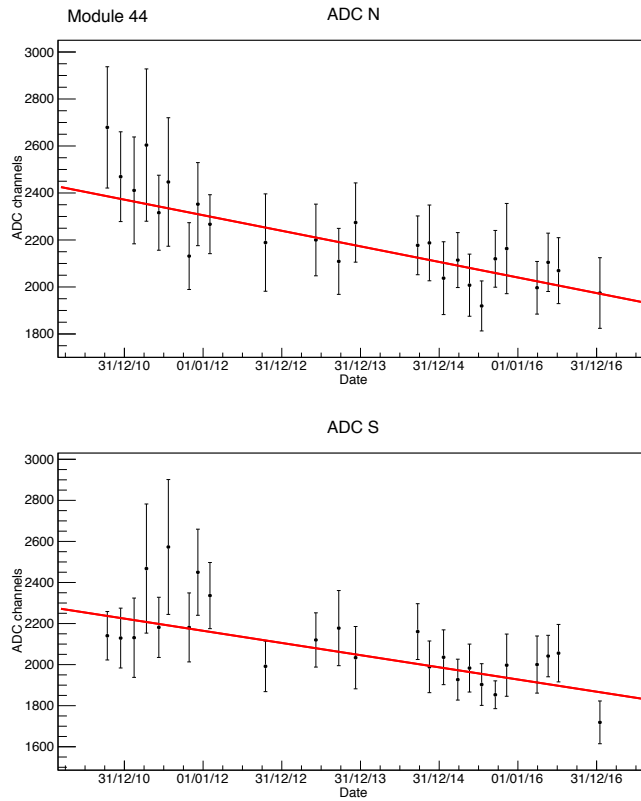
(b)

Figure 5.2.: MPVs over time with linear fits in two example modules. The two upper figures show the MPVs in M6 (top module) and the two lower figures show the MPVs in M44 (bottom module).

5.2. Determination of the detection efficiency

The analysis above shows that the gain of the PMT groups have decreased remarkably since the start of the experiment. However, it doesn't provides a direct measure of the change of the muon detection efficiency. To estimate the detection efficiency, the knowledge of the trigger threshold of each module is needed. Before the experiment, the scintillator modules have been calibrated using cosmic muons [Hab04]. Due to the aging effects of the modules, the trigger threshold must be determined again. As the muon flux in the underground laboratory is reduced significantly, the cosmic muons cannot be used for calibration anymore. In this section, an alternative approach to determine the trigger threshold is described. The detection efficiencies in different time periods are derived using the obtained threshold values.

5.2.1. Effective trigger threshold

As discussed in section 3.2, there are two thresholds in the measurement of muon-veto system. One is a digital conversion threshold, which is typically set to 120 ADC channels. The influence of digital threshold on the muon detection efficiency can be neglected, because the MPVs are typically above 1000 ADC channels and the Landau distribution falls quickly towards the low energy region.

The trigger threshold, on the other hand, is relevant for the following analysis. It is a hardware threshold which is set to 150 mV. Only the pulse with an amplitude above this value triggers the data acquisition. Although the hardware threshold is set to same voltage in each module, the value in ADC channels depends on the gain of the individual PMT groups. Thus the value of trigger threshold is different in each module.
Additionally, it depends on the shape of measured pulse, as the ADC value is the integral of a signal. For example, a flat pulse has a larger energy deposit than a steep pulse with same amplitude. The pulse shape also depends on the light propagation and is thus position dependent. However, a calibration source is needed to determine the position dependency of trigger threshold, which is not performed in this work.

Averaging over the module length, the effective trigger threshold is expected to be a curve instead of a step function. The efficiency of a module can be given as a function of energy, which is low for low energy deposit and is expected to be 100% in high energy region. It is similar to the behaviour of an error function:

$$\text{erf}(x) = \frac{2}{\sqrt{\pi}} \int_0^x e^{-t^2} \, \mathrm{d}t \tag{5.1}$$

It describes the convolution of a Heaviside function $\Theta(x)$ with a Gaussian distribution. By shifting and rescaling, the error function is able to imitate the behaviour of the actual detection efficiency curve at the threshold. It is characterised by two parameters, the effective threshold E_{thr} and the standard deviation σ. The effective trigger threshold is defined as the ADC value where detection efficiency is 50% and the σ describes the smearing effect of the spectrum.

Method of effective trigger threshold determination

When a module is triggered, all the non-zero signals in the muon-veto system are stored. It is therefore possible to analyse the the events for a certain module I even if they don't trigger the module I. For the analysis of one PMT group X in module I, the ADC values of all the events that have triggered another module J are stored in histogram H1. In contrast to the condition of muon selection, which requires both non-zero TDC values, the trigger condition of a PMT group X used in the following analysis requires only that the TDC

on the same side has a non-zero value. Requiring both TDC channels will introduce a dependency on the PMT group on the other side, while the trigger threshold is determined separately for two ends of a module. The events with one TDC trigger are stored in histogram H2. The efficiency of one PMT group is determined by the division of H2 and H1.
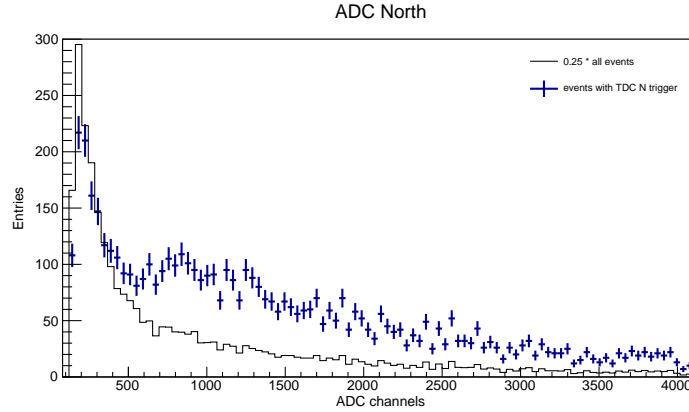
(a) Example of the spectrum with and without trigger condition of ADC N in M6. The data points (blue) are events which satisfy the trigger condition in the same end (Northern PMT group). The spectrum of all events (black) are scaled by a factor of 4.
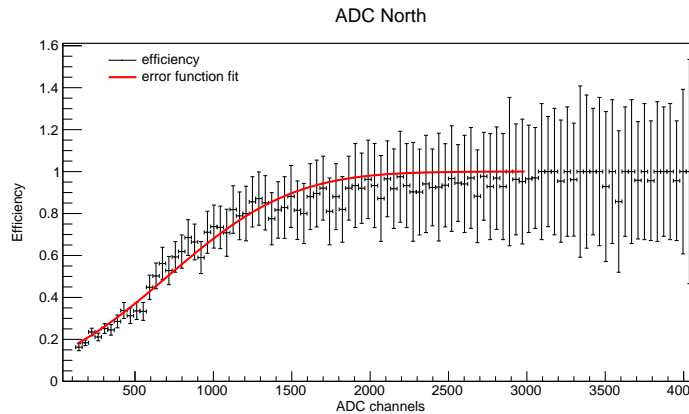
(b) Histogram of events triggering the PMT group on the same side divided by all events with error bars (black) and the error function fit (red).

Figure 5.3.: Example of the method to determine the effective trigger threshold of a PMT group.

Fig. 5.3 shows an example of this method. The events that triggered one PMT group are plotted with all events. As expected, the detection efficiency increases with ADC values and goes toward 100%. As can be seen in the figure, the increase is slightly asymmetric: it is more rapid at first and is then flatter. The estimation with an error function is therefore conservative for low energy events and optimistic for high energy events.

The effective trigger threshold in ADC units are calculated for each PMT group in different time periods. To increase statistics, several runs are combined to perform the error function fit. Run 70-79 (year 2010) are investigated for the early time period and Run 124-138 (year 2015-2017) for the late time period. The results are listed in tab. 5.2 in the following section.

5.2.2. Detection efficiency of a module

In addition to the above criteria, events with a coincidence in adjacent modules are excluded. These events have a higher probability to be induced by secondary particles or grazing muons. They mostly have low energy deposits, where the efficiency is also low due to the trigger threshold, and can lead to a decrease of total detection efficiency.
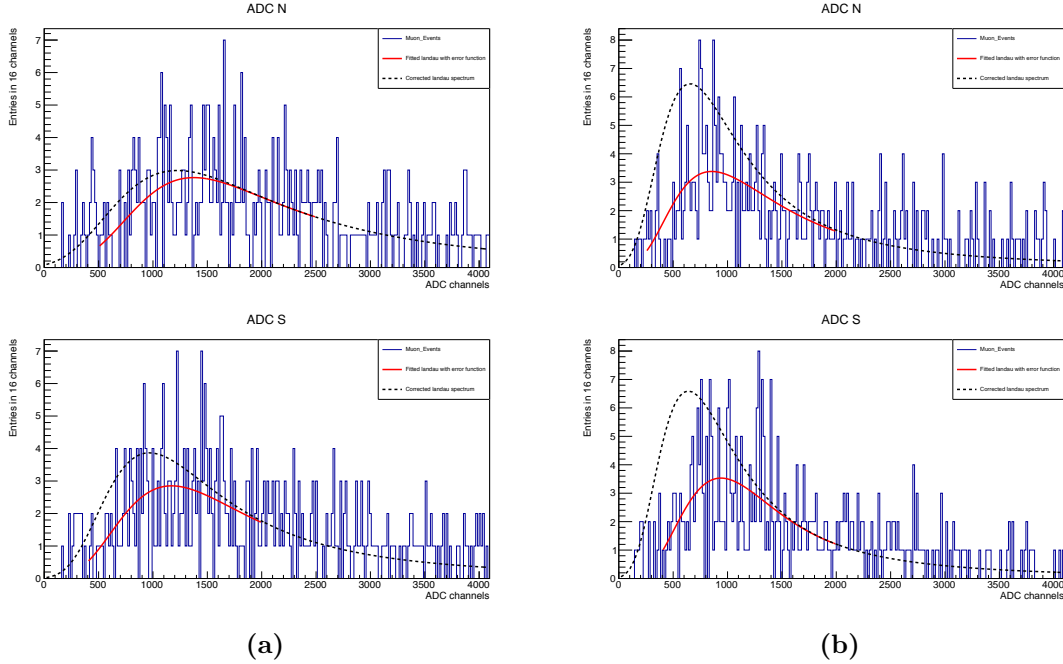
Figure 5.4.: Spectrum of muon-induced events in M6 in earlier runs (left) and latest runs (right). The spectra are fitted with a Landau distribution with an error function (red). The corrected spectrum (black, dotted) is determined by dividing the error function.

The muon energy deposit can be described with a Landau distribution, whereas the measured energy deposit is dependent on the response of the individual modules. Therefore, the ADC spectrum is expected to be a Landau multiplied by an error function. The selected data are fitted with this function and the corrected spectrum is given by a Landau distribution with the obtained parameters from the fit (see fig. 5.4). The efficiency can be determined by the integral of the spectrum with and without the error function. The results for selected modules are listed in tab 5.2, the complete table is given in appendix A.

For each PMT group, three efficiency values are given. $\epsilon_{20\%}$ integrates from the energy where the entries are equal to 20% of the entries at MPV. ϵ_{MPV} integrates from the MPV and gives a optimistic estimation. Therefore, the total efficiency of a module is given by the product of $\epsilon_{50\%\mathrm{MPV}}$ in two PMT groups, for which the spectrum is integrated from half of the energy at MPV.

For some of the PMT groups, the spectrum cannot be fitted properly (for example fig.5.5). The efficiency is estimated by the other PMT group in the same module. If the fit method cannot be applied for both PMT groups, the total detection efficiency is given by the mean values of other modules on the same side.

As expected, the MPV decreased and the trigger threshold increased in the time period of seven years, which lead to a loss of detection efficiency. Most modules show a relative decrease of 30%. Although the relative change is significant, the absolute values of detection efficiency should only be used as lower limits, since they are strongly underestimated. An analysis in 2010 using similar method obtained the result $\epsilon_{\mathrm{M6}} = 0.88$ and $\epsilon_{\mathrm{M36}} = 0.96$ [Nie10], showing that the efficiency values derived here are indeed too conservative.

Table 5.2.: The trigger threshold and detection efficiency of PMT groups in selected modules on different sides of the muon-veto system (for the full table see appendix A). The MPV in this table denotes the most probable value of the Landau distribution with error function. The total efficiency is estimated by the product of the efficiency value $\epsilon_{50\%\mathrm{MPV}}$ of each PMT group, which is determined by the integration from half of the MPV energy.

Module	End	MPV	Threshold	σ_{erf}	$\epsilon_{20\%}$	$\epsilon_{50\%\mathrm{MPV}}$	ϵ_{MPV}	$\epsilon_{\mathrm{tot},50\%\mathrm{MPV}}$
			in ADC channels					
M6	N	1401	532	737	0.86	0.90	0.97	
early	S	1256	615	712	0.83	0.86	0.95	0.77
M6	N	872	707	627	0.67	0.71	0.85	
late	S	975	746	416	0.60	0.75	0.94	0.53
M15	Nemo	2674	560	143	0.99	1.00	1.00	
early	Est	1292	186	13	1.00	1.00	1.00	1.00
M15	Nemo	1713	1879	758				
late	Est	1284	958	280	0.73	0.77	0.99	0.59
M17	B	1200	515	112	0.99	1.00	1.00	
early	H	1043	100	740	0.88	0.94	0.98	0.94
M17	B	1457	855	384	0.82	0.90	0.99	
late	H	1359	671	611	0.72	0.89	0.98	0.80
M36	Est	1452	912	803	0.61	0.80	0.93	
early	Nemo	1346	821	568	0.79	0.83	0.96	0.67
M36	Est	1201	1114	624	0.48	0.62	0.85	
late	Nemo	1373	1060	531	0.61	0.72	0.93	0.45
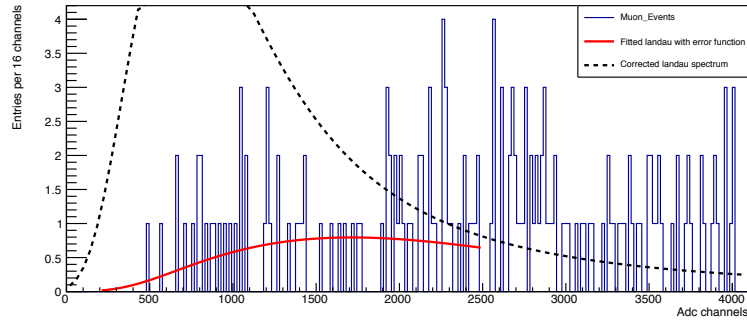
Figure 5.5.: Example of a failed fit of PMT Nemo in M15 in Run124-138. The efficiency is given by the other PMT group in the same module.

The underestimation results from the following facts. First of all, there are still contributions of secondary particles or backgrounds to the low energy region despite the cuts applied. The obtained MPVs from fit are thus smaller and it leads to a smaller detection efficiency.

Secondly, the gain of two PMT groups are considered as uncorrelated for the matter of simplification, while they are correlated in reality. As shown in section 3.2, the light yield measured in near PMT group is larger than the one in far PMT group. This leads to an overestimation for near end and underestimation for far end. Since the efficiency decreases drastically in low energy region, the total detection efficiency is expected to be underestimated. However, the effect of correlation cannot be implemented due to the low statistics of muon events.

Additionally, the muons passing through the muon-veto system have a second chance to be detected when leaving the system. Also, they can partly be detected by measuring the particle showers. Last but not least, the grazing muons, which go through adjacent modules and deposit energy well below MPV, are possible to be detected in both modules. To conclude, the absolute value of detection efficiency derived here should be treated as lower limit and the total efficiency of the muon-veto system is higher as the one of individual modules.

The result shows that the detection efficiency for most of the modules has decreased significantly. Despite that the rate of μ-induced WIMP-like signals is estimated to be low, it can limit the sensitivity of WIMP search if the efficiency of muon-veto system drops. To retain a high detection efficiency as the start of the experiment, the HV applied on individual PMT groups should be increased. By doing so, the gain of PMT groups increases, corresponding to a higher MPV in ADC units and lower effective threshold.

6. Conclusions

The goal of the EDELWEISS-III experiment is to probe the WIMP-nucleon cross-section down to the order of 10^{-9} pb. To achieve such sensitivity, the detectors are enclosed by multiple layers of shielding to reduce backgrounds. The through going muons which can induce WIMP-like signals are tagged with a muon-veto system.

The goal of the this thesis is to investigate the behaviour of the muon-veto system during the time period of seven years since the start of the EDELWEISS-III experiment. The total data obtained by the muon-veto system in seven years from Run70 to Run138 has been analysed.

First, the LED events are analysed for the four extra modules. By comparing change of the mean ADC values from three LEDs on the same module, the contributions of different effects to the aging of module are discussed. The two PMT groups of one module are found to have aged symmetrically. The change of ADC values due to the aging of the scintillator material are derived to be ≈ 3 channels/month for Module 8. This value is expected to be higher for other long modules.
Secondly, muon events are selected for all 46 modules. A strict cut requiring coincidence in more than two modules with full information is applied to get a clean energy spectrum. The change of MPVs from the measured muon energy deposit are investigated. For the four extra modules, the result is consistent with the one obtained from the LED events. For other long modules, the change of MPV in ADC units is typically ≈ 5 channels/month.

Due to the low muon rate in underground laboratory, muons cannot be used to determine the trigger threshold of a module. An alternative method is performed using the events that have triggered another module. However, the position dependent response of modules cannot be derived in this work. A calibration source is needed to determine the position dependency of trigger threshold in individual modules. Averaging over the module length, the effective trigger threshold is derived for each PMT group. The response is described by an error function parametrized by E_{thr} and σ.

The muon energy deposit spectrum is then fitted with a Landau distribution and error function with parameters obtained from the threshold determination. The detection efficiency of each PMT group in different time periods is derived. The obtained values give a lower limit on the detection efficiency of individual modules. For most of the modules, a relative decrease of 30% is observed.

The sensitivity of WIMP-search can be potentially limited by the μ-induced neutron backgrounds, if the total detection efficiency of the muon-veto system decreases significantly. Therefore, the HVs applied on the modules must be adjusted regularly to ensure that the efficiency of individual module remains stable.

Appendix

A. Detection Efficiency

Table A.1.: The determined trigger threshold and detection efficiency of each module in Run70-79 (2010). For some PMT groups, the spectrum cannot be fitted properly and no efficiency value can be derived. The detection efficiency is estimated by the other PMT group in the same module, or the mean value of the modules on the same side if both spectra of PMT groups cannot be fitted.

Module	End	MPV	Threshold	σ_{erf}	$\epsilon_{20\%}$	$\epsilon_{50\%\mathrm{MPV}}$	ϵ_{MPV}	$\epsilon_{\mathrm{tot},50\%\mathrm{MPV}}$
			in ADC channels					
Top								
M1	N	1036	939	690	0.66	0.65	0.80	
	S	827	191	2193	0.69	0.71	0.75	0.4
M2	N	625	786	1622	0.56	0.60	0.66	
	S	214	829	1905	0.53	0.55	0.57	0.33
M3	N	647	494	98	0.88	0.83	1.00	
	S	918	635	136	0.90	0.90	1.00	0.75
M4	N	352	880	194				
	S	355	890	157				0.71
M5	N	1197	554	865	0.79	0.84	0.93	
	S	1108	645	607	0.78	0.83	0.94	0.70
M6	N	1401	532	737	0.86	0.90	0.97	
	S	1256	615	712	0.83	0.86	0.95	0.77
M7	N	1080	190	366	0.97	0.99	1.00	
	S	941	202	223	0.98	0.99	1.00	0.98
M8	N	1443	638	155	0.99	0.99	1.00	
	S	2217	251	101	0.98	1.00	1.00	0.99
N1-North								
M9	B	1320	751	791	0.71	0.82	0.93	
	H	3000	100	1282	0.86	0.97	1.00	0.80
M10	B	650	476	910	0.68	0.76	0.84	
	H	1410	100	989	0.87	0.93	0.98	0.71
M11	B	1133	685	409	0.82	0.86	0.98	
	H	952	493	176	0.94	0.97	1.00	0.83
M12	B	881	660	120	0.92	0.86	1.00	
	H	1140	395	146	0.97	1.00	1.00	0.86
M13	B	799	122	1184	0.79	0.85	0.90	
	H	1331	298	784	0.84	0.94	0.98	0.80
M14	B	1118	836	489	0.73	0.75	0.92	
	H	1138	100	1729	0.77	0.82	0.87	0.61
M15	Nemo	2674	560	143	0.99	1.00	1.00	
	Est	1292	186	13	1.00	1.00	1.00	1.00
N1-South								

M16	Nemo	2481	267	91	0.99	1.00	1.00	1.00
	Est	2451	296	103	0.98	1.00	1.00	
M17	B	1200	515	112	0.99	1.00	1.00	0.94
	H	1043	100	740	0.88	0.94	0.98	
M18	B	893	692	1254	0.65	0.69	0.78	0.69
	H	2184	517	153	0.97	1.00	1.00	
M19	B	1207	587	146	0.97	0.98	1.00	0.98
	H	1799	533	146	0.99	1.00	1.00	
M20	B	2133	1352	1343	0.55	0.72	0.87	0.63
	H	1476	687	639	0.74	0.90	0.98	
M21	B	1117	701	841	0.65	0.79	0.91	0.66
	H	1219	529	1024	0.73	0.84	0.92	
M22	B	442	1156	349				0.82
	H	396	1008	227				
N1-Nemo								
M25	N	349	100	745	0.78	0.83	0.87	0.64
	S	1261	708	1196	0.69	0.77	0.87	
M26	N	488	355	866	0.70	0.77	0.83	0.54
	S	1202	1005	1117	0.56	0.70	0.82	
M27	N	1139	1110	810	0.60	0.61	0.77	0.36
	S	1035	1104	941	0.58	0.58	0.71	
M28	N	339	879	1238	0.51	0.55	0.59	0.33
	S	958	1075	856	0.45	0.60	0.76	
N1-East								
M29	N	696	1289	836	0.31	0.41	0.56	0.25
	S	1334	1253	1137	0.59	0.62	0.76	
M30	N	1166	1269	998	0.56	0.57	0.70	0.33
	S	816	1054	1184	0.52	0.57	0.67	
M31	N	1142	1164	847	0.58	0.59	0.75	0.34
	S	504	969	1574	0.54	0.58	0.63	
M32	N	466	1387	1456	0.41	0.46	0.51	0.19
	S	340	1338	1263	0.37	0.41	0.46	
N0-East								
M33	N	1031	593	264	0.86	0.93	1.00	0.87
	S	1404	755	321	0.91	0.94	1.00	
M34	N	1091	1459	1129				0.87
	S	1157	1404	852				
M35	N	1125	1723	1192				0.87
	S	1016	1557	1039				
N0-South								
M36	Est	1452	912	803	0.61	0.80	0.93	0.67
	Nemo	1346	821	568	0.79	0.83	0.96	
M37	Est	1411	730	505	0.77	0.90	0.99	0.80
	Nemo	1329	746	425	0.85	0.89	0.99	
M38	Est	1446	1247	1167	0.61	0.65	0.79	0.35
	Nemo	1223	1293	700	0.54	0.54	0.75	
N0-North								
M39	Est	1570	967	734	0.74	0.81	0.95	0.61
	Nemo	1156	876	484	0.75	0.75	0.92	
M40	Est	1208	1098	913	0.62	0.64	0.79	0.43
	Nemo	1243	1064	721	0.66	0.67	0.84	
N0-Nemo								
M41	N	1476	879	973	0.77	0.78	0.90	0.57

	S	1238	903	853	0.72	0.73	0.86	
M42	N	1262	934	631	0.73	0.74	0.90	
	S	1036	817	648	0.68	0.72	0.87	0.53
M43	N	988	1448	1336	0.46	0.49	0.60	
	S	632	676	1566	0.63	0.68	0.73	0.33
Bottom								
M44	Est	2772	521	103	1.00	1.00	1.00	
	Nemo	2757	541	123	1.00	1.00	1.00	1.00
M45	Est	1193	1327	962	0.56	0.55	0.69	
	Nemo	994	1141	741	0.54	0.54	0.69	0.30
M46	Est	1687	1231	846	0.72	0.73	0.89	
	Nemo	1479	899	788	0.78	0.80	0.93	0.58
M47	Est	1893	1036	628	0.86	0.88	0.98	
	Nemo	1400	1000	422	0.81	0.81	0.96	0.71
M48	Est	2642	713	345	0.99	1.00	1.00	
	Nemo	2780	614	196	1.00	1.00	1.00	1.00

Table A.2.: The determined trigger threshold and detection efficiency of each module in Run124-138 (2015-2017). For some PMT groups, the spectrum cannot be fitted properly and no efficiency value can be derived. The detection efficiency is estimated by the other PMT group in the same module, or the mean value of the modules on the same side if both spectra of PMT groups cannot be fitted.

Module	End	MPV	Threshold in ADC channels	σ_{erf}	$\epsilon_{20\%}$	$\epsilon_{50\%\text{MPV}}$	ϵ_{MPV}	$\epsilon_{\text{tot},50\%\text{MPV}}$
Top								
M1	N	1010	1403	1291	0.49	0.49	0.57	
	S	244	1180	1908	0.47	0.49	0.51	0.24
M2	N	347	1702	1799	0.35	0.38	0.41	
	S	187	1865	2044	0.32	0.33	0.35	0.13
M3	N	112	676	285				
	S	140	800	307				0.54
M4	N	664	609	99				
	S	354	696	114				0.54
M5	N	951	733	604	0.69	0.73	0.88	
	S	881	723	425	0.49	0.72	0.91	0.53
M6	N	872	707	627	0.67	0.71	0.85	
	S	975	746	416	0.60	0.75	0.94	0.53
M7	N	937	407	332	0.90	0.94	0.99	
	S	838	329	184	0.98	0.98	1.00	0.92
M8	N	1779	926	339	0.92	0.95	1.00	
	S	1229	680	313	0.86	0.93	1.00	0.88
N1-North								
M9	B	1079	1154	586	0.28	0.53	0.79	
	H	2170	354	1769	0.76	0.86	0.93	0.46
M10	B	1027	886	637	0.49	0.69	0.87	
	H	2600	344	1104	0.84	0.96	0.99	0.66
M11	B	1073	956	160				
	H	961	932	160				0.56
M12	B	970	873	140				
	H	1028	803	158	0.84	0.77	1.00	0.59
M13	B	1162	811	700	0.59	0.78	0.92	
	H	1115	757	694	0.68	0.77	0.91	0.60
M14	B	150	1300	567				
								0.48

	H	1196	995	1290	0.58	0.69	0.80	
M15	Nemo	1713	1879	758				
	Est	1284	958	280	0.73	0.77	0.99	0.59

N1-South

M16	Nemo	864	644	240	0.69	0.78	0.98	
	Est	1192	853	547	0.55	0.77	0.94	0.60
M17	B	1457	855	384	0.82	0.90	0.99	
	H	1359	671	611	0.72	0.89	0.98	0.80
M18	B	1385	1260	636	0.37	0.60	0.86	
	H	1818	1228	658	0.66	0.78	0.96	0.47
M19	B	931	614	188	0.88	0.90	1.00	
	H	1403	538	162	0.98	1.00	1.00	0.90
M20	B	1003	1616	1464	0.40	0.50	0.60	
	H	1333	859	540	0.63	0.82	0.96	0.41
M21	B	1000	785	434	0.52	0.73	0.93	
	H	1131	733	577	0.62	0.81	0.95	0.59
M22	B	704	647	124				
	H	637	448	86	0.95	0.93	1.00	0.86

N1-Nemo

M25	N	409	561	522	0.50	0.59	0.71	
	S	1182	1199	704	0.36	0.58	0.81	0.34
M26	N	800	844	470	0.35	0.58	0.81	
	S	1114	1297	604	0.28	0.45	0.74	0.26
M27	N	1380	1349	659	0.48	0.55	0.82	
	S	1071	1398	755	0.45	0.45	0.61	0.25
M28	N	1072	1158	817	0.44	0.58	0.76	
	S	1029	1318	695	0.42	0.44	0.66	0.26

N1-East

M29	N	1107	1191	508	0.41	0.47	0.78	
	S	1135	1235	606	0.46	0.50	0.76	0.24
M30	N	2133						
	S	546						0.26
M31	N	1152	1364	664	0.42	0.45	0.70	
	S	1598	1509	931	0.45	0.59	0.80	0.27
M32	N	410	1789	997				
	S	945	1708	798				0.26

N0-East

M33	N	972	601	225	0.87	0.91	1.00	
	S	1321	765	285	0.93	0.93	1.00	0.85
M34	N	1033	1798	947				
	S	946	1697	813				0.85
M35	N	1051						
	S	849						0.85

N0-South

M36	Est	1201	1114	624	0.48	0.62	0.85	
	Nemo	1373	1060	531	0.61	0.72	0.93	0.45
M37	Est	1383	924	550	0.79	0.80	0.95	
	Nemo	1283	902	467	0.77	0.79	0.95	0.63
M38	Est	1266	1445	740	0.25	0.48	0.74	
	Nemo	831	986	465	0.22	0.46	0.75	0.22

N0-North

M39	Est	1650	1046	542	0.78	0.83	0.98	
	Nemo	1145	885	392	0.74	0.75	0.94	0.62

M40	Est	945	1314	965	0.47	0.47	0.58	0.25
	Nemo	1042	1213	803	0.53	0.53	0.68	
N0-Nemo								
M41	N	1314	1495	974	0.50	0.52	0.69	0.24
	S	996	1338	828	0.42	0.46	0.64	
M42	N	1494	1605	908	0.49	0.51	0.73	0.24
	S	1024	1358	893	0.47	0.47	0.60	
M43	N	875						0.24
	S	261	1898	1085				
Bottom								
M44	Est	1990	1147	428	0.86	0.90	1.00	0.79
	Nemo	1891	1172	403	0.85	0.88	1.00	
M45	Est	804	1273	874	0.42	0.42	0.52	0.16
	Nemo	665	1260	871	0.37	0.37	0.46	
M46	Est	1415	1256	483	0.63	0.62	0.88	0.38
	Nemo	1400	1245	525	0.63	0.62	0.87	
M47	Est	1439	1275	515	0.59	0.60	0.88	0.33
	Nemo	1307	1248	452	0.56	0.55	0.85	
M48	Est	1754	1217	467	0.80	0.80	0.98	0.71
	Nemo	1955	1162	430	0.87	0.89	1.00	

Bibliography

[A+17]   E. Armengaud et al. Performance of the EDELWEISS-III experiment for direct
           dark matter searches. *J. Instrum.*, 12, 2017.

[BR97]   Rene Brun and Fons Rademakers. ROOT - An object oriented data anal-
           ysis framework. *Nucl. Instruments Methods Phys. Res. Sect. A Accel.
           Spectrometers, Detect. Assoc. Equip.*, 389(1-2):81–86, 1997.

[CAA+12]   G A Cox, E Armengaud, C Augier, A Benoit, et al. A multi-tiered data
           structure and process management system based on ROOT and CouchDB.
           *Nucl. Instruments Methods Phys. Res. Sect. A Accel. Spectrometers, Detect.
           Assoc. Equip.*, 684:63–72, 2012.

[CBG+06]   Douglas Clowe, Maruša Bradač, Anthony H Gonzalez, et al. a Direct Empirical
           Proof of the Existence of Dark Matter 1. *Astrophys. J.*, 648:109–113, 2006.

[Col16]   Planck Collaboration. Planck 2015 results. *Astron. Astrophys.*, 13, 2016.

[DBC+01]   P. Di Stefano, L. Bergé, B. Chambon, M. Chapellier, et al. Background
           discrimination capabilities of a heat and ionization germanium cryogenic detector.
           Astropart. Phys., 14(4):329–337, 2001.

[Hab04]   F Habermehl. Entwicklung der Datenaufnahme und Tests der Vetomodule für
           das EDELWEISS II muon-Vetozählersystem, 2004.

[Kéf16]   Cécile Kéfélian. *Search for dark matter with EDELWEISS-III excluding back-
           ground from muon-induced neutrons.* PhD thesis, 2016.

[Klu13]   Holger Martin Kluck. *Measurement of the cosmic-induced neutron yield at the
           Modane underground laboratory.* PhD thesis, 2013.

[Lan44]   L. Landau. On the energy loss of fast particles by ionization. *USSR J. Phys.*,
           8(4):201–205, 1944.

[Mil83]   M. Milgrom. A modification of the Newtonian dynamics as a possible alternative
           to the hidden mass hypothesis. *Astrophys. J.*, 270:365, 1983.

[Nie10]   Holger Nieder. Bestimmung des Flusses kosmischer Myonen durch das Edelweiss-
           II Experiment, 2010.

[PQ77]   R. D. Peccei and Helen R. Quinn. CP conservation in the presence of
           pseudoparticles. *Phys. Rev. Lett.*, 38(25):1440–1443, 1977.

[Rei98]   J Reichenbacher. Untersuchung der optischen Eigenschaften grossflächiger
           Plastikszintillatoren für den KARMEN-Upgrade, 1998.

[RTF80]   V. C. Rubin, N. Thonnard, and Jr. Ford, W. K. Rotational properties of 21
           SC galaxies with a large range of luminosities and radii, from NGC 4605 /R =
           4kpc/ to UGC 2885 /R = 122 kpc/. *Astrophys. J.*, 238:471, 1980.

[SAA⁺13] B. Schmidt, E. Armengaud, C. Augier, A. Benoit, et al. Muon-induced background in the EDELWEISS dark matter search. *Astropart. Phys.*, 44:28–39, 2013.

[Sch13] V Schipperges. Vermessung der Auslesetotzeit des EDELWEISS-3 Myon-Veto-Systems, 2013.